Research Article | Vol. 27, No. 20 / 30 September 2019 / Optics Express 28239
Optics EXPRESS

Wavelength dependent characterization of a multimode fibre endoscope

TOMÁŠ PIKÁLEK,[1] JOHANNA TRÄGÅRDH,[1,*] STEPHEN SIMPSON,[1] AND TOMÁŠ ČIŽMÁR[1,2]

[1] *Institute of Scientific Instruments of the Czech Academy of Sciences, Královopolská 147, 61264 Brno, Czech Republic*
[2] *Leibniz Institute of Photonic Technology, Albert-Einstein-Straße 9, 07745 Jena, Germany*
[*] *johanna@isibrno.cz*

Abstract: Multimode fibres have recently shown promise as miniature endoscopic probes. When used for non-linear microscopy, the bandwidth of the imaging system limits the ability to focus light from broadband pulsed lasers as well as the possibility of wavelength tuning during the imaging. We demonstrate that the bandwidth is limited by the dispersion of the off-axis hologram displayed on the SLM, which can be corrected for, and by the limited bandwidth of the fibre itself. The selection of the fibre is therefore crucial for these experiments. In addition, we show that a standard prism pulse compressor is sufficient for material dispersion compensation for multi-photon imaging with a fibre endoscope.

1. Introduction

For applications such as tumour diagnosis deep in tissue or for studying the formation of neuronal connections in the brain *in vivo*, a new type of optical endoscope providing minimally invasive imaging with a sub-micrometre resolution is needed. Current non-optical, non-invasive methods, such as CT or MRI, have insufficient resolution whereas standard optical micro-endoscopes have a too large footprint to be optimal for imaging applications such as *in vivo* brain imaging. Multimode fibres have shown promise as minimally invasive high-resolution endoscopes [1,2], and recently, even *in vivo* imaging [3–5] has been demonstrated. By using advanced wavefront shaping methods [6,7], we can transform the multimode fibre into an ultrathin (<100 µm) laser-scanning microscope. In essence, shaping the input wave-front adjusts the relative phase offsets and amplitudes of the propagation modes in the fibre, so that the speckle pattern, associated with the transport of coherent light through the fibre, is turned into a diffraction limited focus with a controllable position [8].

In terms of technology, the field of multimode fibre endoscopy has progressed from basic fluorescence imaging [9,10], to more advanced imaging methods such as dark-field microscopy [9], light-sheet microscopy [11], wide-field imaging [12] and Raman microscopy [13,14]. Also non-linear imaging, such as basic two-photon fluorescence imaging and laser ablation using a multimode fibre endoscope have been demonstrated [15–17]. For non-linear imaging methods, multiple wavelengths must be simultaneously focused to allow focusing of femtosecond laser pulses at the sample plane. Since the shape of the propagation modes in the fibre, as well as their propagation constants vary with wavelength, the bandwidth of the fibre will be finite. In addition, the pulse length should be kept short, which requires dispersion compensation, that might vary across the fibre facet. Moreover, non-linear imaging methods such as coherent anti-Stokes Raman scattering (CARS), which is highly relevant for e.g. employing the multimode fibre endoscope as a minimally invasive tool for diagnosing tumours [18], potentially require that the excitation wavelength can be tuned during the experiment, which also requires that the bandwidth of the fibre is high. However, it is not clear how to choose a graded-index fibre with sufficient bandwidth, since manufacturers specify the bandwidth of graded-index fibres in units

#373219 https://doi.org/10.1364/OE.27.028239
Journal © 2019 Received 22 Jul 2019; revised 28 Aug 2019; accepted 1 Sep 2019; published 19 Sep 2019

Optics EXPRESS

of MHz·km, based on differential modal delay measurements, and it is not obvious how this translates to their performance as imaging fibre endoscopes.

Here, we investigate the bandwidth of the focal spot created at the distal end of the fibre for a step-index fibre and a number of graded-index fibres when used as a point scanning imaging devices. We also demonstrate that it is necessary to compensate for the wavelength dispersion inherent in wavefront shaping based on an SLM in an off-axis configuration, in order to make full use of the fibre bandwidth. Using a prism placed in a conjugate plane to the SLM, which is suitable for compensating the dispersion when using broadband light such as a femtosecond pulsed laser, a bandwidth of 34 nm (for a 0.3 NA fibre) could be achieved.

Furthermore, in order to investigate what type of dispersion compensation is required to minimize the pulse width, we measure the spectral phase at the focal plane for different focal spot positions. We show that, in fact, despite the seemingly complicated wavefront-shaping scheme, the measured group velocity dispersion (GVD) was constant across the fibre facet. This implies that a standard and simple method for dispersion compensation, such as a prism compressor, can be used for multi-photon imaging with a fibre endoscope.

This paper thus provides much-needed advice on the practical implementation of multi-photon imaging in multimode fibre endoscopes, regarding the choice of fibres and the dispersion compensation of the system.

2. Methods

2.1. Experimental setup

A schematic of the experimental setup is shown in Fig. 1. The laser used for the measurements of the fibre bandwidth was a tunable CW TiS laser with a bandwidth of <100 kHz (SolsTiS SA PSX F, MSquared). For investigating focusing of broadband pulses through the fibres a tunable femtosecond laser (Chameleon Discovery, Coherent) was used.

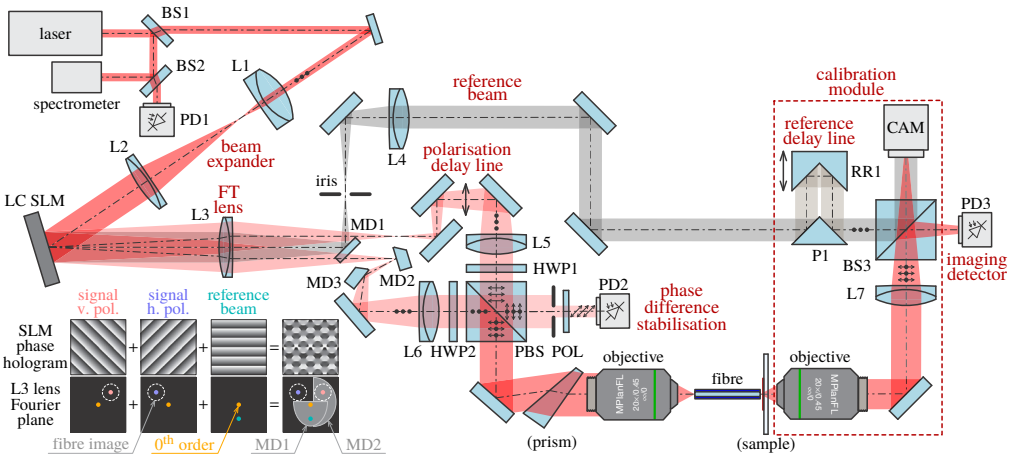

Fig. 1. Experimental setup used for fibre characterization. LC SLM – liquid crystal spatial light modulator, L – lens, PD – photodiode, BS – non-polarising beamsplitter, MD – D-shaped mirror, HWP – half-wave plate, PBS – polarising beamsplitter, POL – polariser, CAM – camera, P – right-angle prism mirror, RR – roof prism mirror. The inset shows hologram generation and the corresponding focused points at the Fourier plane of the modulator as well as how the mirrors MD1 and MD2 pick off the signal for the reference and the vertical polarisation, respectively.

Optics EXPRESS

Part of the beam was picked off using a beamsplitter (BS1) and sent to a spectrometer and a photodiode for monitoring the power (PD1). The beam was then expanded using a pair of achromatic lenses onto a phase-only liquid crystal spatial light modulator (HSP1920-1064-HSP8, Meadowlark Optics). The beam significantly overfilled the SLM creating a near-uniform light distribution. For the experiments, the phase hologram displayed on the SLM was multiplied by a Gaussian aperture with a diameter corresponding to the numerical aperture of the fibre. The Fourier plane of the SLM created by an achromatic lens (L3) was then imaged using a 4*f* system, through the optics controlling the polarisation (described below), onto the fibre input facet.

In contrast to low-NA step-index fibres, which preserve circular polarisation [19], the graded-index fibres used here completely scrambled the polarisation of the input light, resulting in distinctly different speckle patterns for the different polarisations [16]. Thus, to minimise the optical power in the speckle pattern around the focused spot, which is inherent in imaging through multimode fibres, the polarisation of the light coupled into the fibre had to be controlled. This was achieved by using two separate patterns on the SLM, directing the beam into two different areas in the Fourier plane (see inset in Fig. 1). The two beams were then separated using a D-shaped mirror (MD2) and collimated using achromatic lenses (L5, L6). An achromatic half-wave plate (HWP1) was used in one of the beams to rotate the polarisation. In the other beam, a second half-wave plate of the same type (HWP2) was placed in order to minimise the difference in material dispersion between the two beam paths. The beams were then combined using a polarising beamsplitter cube (PBS). For the purpose of focusing femtosecond pulses and spectral phase measurements, the path length difference of the two polarisation paths was adjusted to close to zero using a delay stage in one of the branches. The focus at the distal end of the fibre was created by interference of the two beams, and any phase mismatch between them caused a significant drop in the focusing quality. Therefore, the relative phase difference between the two polarisation paths had to be stabilised. This was achieved by periodically monitoring the relative phase between them using a polariser (POL) with its axis oriented at 45° with respect to the polarisation of both beams and a photodiode (PD2). The phase was measured using phase-shifting interferometry and the phase difference was reset to zero using the SLM. This way, the focusing quality remained constant during laser wavelength tuning and despite any phase drift between the two polarisation paths.

In order to compensate for the chromatic dispersion of the hologram, which is a sum of diffraction gratings displayed on the SLM, a wedge prism (PS812, Thorlabs) could be placed in the beam in a plane conjugated with the SLM [20]. The axis of the prism was rotated by 45° in order to match the dispersion direction (as shown in Fig. 2(b)). The optimal angle of incidence of the beam on the prism, which minimises the dispersion of the setup, depends on the central wavelength and the pitch of the grating displayed on the SLM. Using sequential ray tracing in Zemax, an optimal angle of incidence of 51° was found for a wavelength of 780 nm and a grating pitch of 138 µm.

The beam was focused onto the input facet of a multimode fibre using a 20× objective (MPlanFL N 20×/0.45NA, Olympus), with the SLM imaged to the back focal plane of the objective. The distal end of the fibre was imaged onto a CMOS camera (ace acA1920-155um, Basler) using a second 20× objective and a 200 mm achromatic lens (L7). The camera was focused onto a plane 50 µm in front of the fibre facet. Part of the beam was reflected off a non-polarising beamsplitter cube (BS3) onto a photodiode (PD3) that was used as a bucket detector for imaging in transmission.

The fibre calibration procedure required to use the fibre as a point scanning device involves measuring the phase of the output speckle pattern using phase-shifting interferometry. This requires a reference beam, which was generated by an additional grating on the SLM. The reference beam and the 0^{th} diffraction order were reflected off a D-shaped mirror (MD1) placed near the Fourier plane, and the reference beam was isolated using an iris and collimated using an

Optics EXPRESS

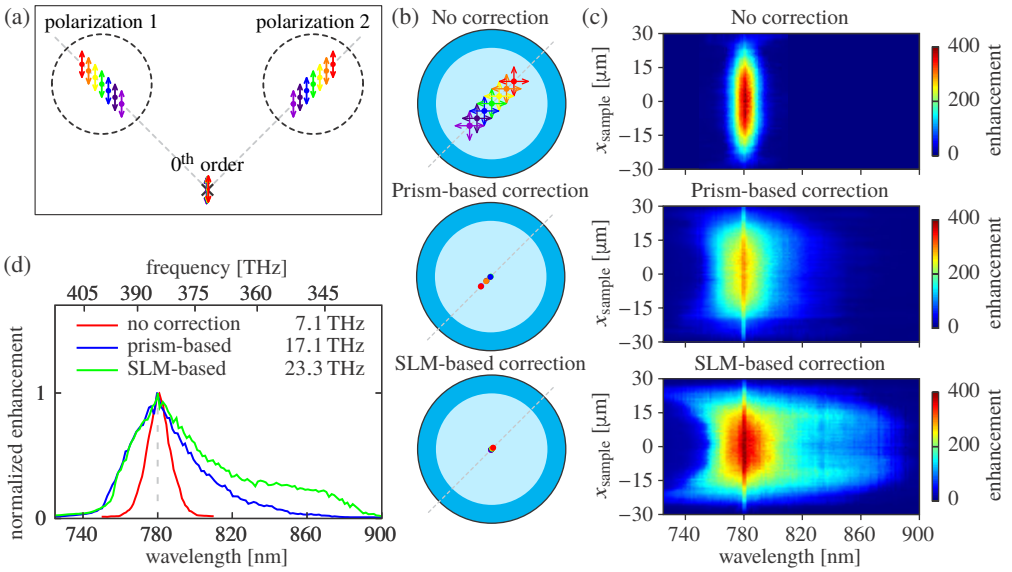

Fig. 2. SLM dispersion compensation. (a) Drawing of the top half of the Fourier plane of the SLM for two gratings creating the two focused points for the two polarisation directions (see inset in Fig. 1). Different wavelengths are represented by different colours. Arrows show polarisation direction and dashed lines represent the image of the fibre core. (b) Focused points at the fibre input facet for different wavelengths without and with the dispersion correction. The arrows showing the polarisation direction are omitted for clarity in the two bottom figures. (c) Intensity enhancement for output points 50 µm in front of the fibre facet at a different position (x_{sample}) along a radius in the focal plane as a function of wavelength when tuning the laser from the calibration wavelength of 780 nm. (d) Comparison of different dispersion compensation methods for a point in the centre of the focal plane. The numbers in the legend are the measured bandwidths calculated as the FWHM of the enhancement measured as a function of the wavelength.

achromatic lens (L4). The reference beam path included a delay line, which was used to set the optical path difference between the signal and reference path to zero for focusing of the pulsed laser and for spectral phase measurement. The signal beam, that had propagated through the fibre, and the reference beam were then overlapped using the non-polarising beamsplitter cube (BS3).

The fibres used in the experiment are listed in Table 1. The fibres were cleaved to a flat facet and mounted in a ferrule with UV curable glue (NOA65, Norland Optical).

Table 1. Parameters of the Fibres Used in the Experiment and Number of Input Points Used for the Calibration.

Fibre	Type	Core	NA	Number of modes	Number of input points
Thorlabs GIF50E	graded-index (OM4)	50 µm	0.20	≈ 400	≈ 4200
Thorlabs GIF50C	graded-index (OM2)	50 µm	0.20	≈ 400	≈ 4200
Thorlabs GIF625	graded-index (OM1)	62.5 µm	0.275	≈ 1200	≈ 6500
Prysmian DrakaElite	graded-index	50 µm	0.29	≈ 850	≈ 4200
Thorlabs FG050LGA	step-index	50 µm	0.22	≈ 980	≈ 4200

Optics EXPRESS

2.2. Fibre calibration procedure

In order to create the foci on the output facet of the fibre, the light transport through the fibre has to be characterized in a calibration procedure. The procedure, in essence, finds the phase relationship between a number of foci on the input facet (input points) needed to achieve constructive interference in a point at the distal end of the fibre (output point). In literature, these foci are often referred to as input and output modes to distinguish them from the fibre propagation modes [8].

The usable range of input points, that is, those that were focused in the core and therefore coupled into the fibre, was found by raster scanning a point across the input facet of the fibre, by displaying consecutive gratings with different pitch on the SLM, and measuring the power transmitted by the fibre by integrating all the pixels corresponding to the fibre core on the camera. Only the points that gave at least 20 % light transmission, relative to the input points near the centre of the fibre, were selected. The number of input points was significantly higher than the number of modes of the fibre (see Table 1). Since the optical setup was designed to accommodate fibres with NA up to 0.36, the input facet was heavily oversampled for all graded-index fibres with low NA. This had, however, no negative impact on the quality of the focus.

The selected input points were then displayed one by one. The resulting speckle pattern in the focal plane in front of the output fibre facet was imaged onto the camera and overlapped with the plane reference wave. Using phase-shifting interferometry, the phase and the amplitude of each output point for each input point were then measured. This procedure was performed for both input polarisations. The polarisation of the reference wave was linear and vertical in both cases, resulting in a linearly polarised output point.

A focused output point in the focal plane was then created by displaying all the phase gratings on the SLM corresponding to the input points simultaneously, with a phase set to the negated phase values and an amplitude set to the amplitude values measured in the desired output point. Thus, constructive interference of all the waves corresponding to the input points was achieved in the output point in the focal plane. The amplitude information suppressed those input points that would not contribute to the interference in the selected output point and would therefore only increase the background.

After the calibration, the quality of the focused output point was evaluated. We calculated the intensity enhancement, here, defined as a ratio between the average intensity in the focused output point (found by thresholding an HDR image of the focal plane at $1/e^2$ of its maximum) and the intensity averaged over the whole calibrated field of view. This is in line with the method used in [6,21,22]. If the enhancement was instead defined as the peak intensity divided by the average intensity, the calculated enhancement values would, for an Airy spot, increase by a factor of 2.2, but since it is a constant scaling factor, the retrieved bandwidths would remain the same. In addition, the FWHM of the size of the output point was calculated by fitting an Airy disc to the HDR image of the focal plane.

In literature, the power ratio is often used to evaluate the quality of the focused point created by controlling the light transmission through the multimode fibre [1]. This quantity is defined as a ratio between the power in the output point and the total power transmitted by the fibre into the focal plane. For a phase-only modulation, a theoretical limit of $\pi/4 \approx 79$ % is often stated [8] with the remaining $\approx$21 % of the power randomly distributed in the speckle background. Although this quantity gives an easy to understand measure of the fraction of light correctly focused to the spot, it is problematic to use it with the data presented here. The power ratio calculation usually involves fitting a theoretical function, usually an Airy disc, to the intensity distribution in the focal plane in order to estimate the power in the spot itself. The selection of the model function then significantly affects the results. Moreover, while for wavelengths close to the calibration wavelength this procedure successfully fitted the spots and for the calibration wavelength the calculated power ratios reached the theoretical limit (as shown in Fig. 4(a)) a high

Optics EXPRESS

speckle background around spots after a larger wavelength tuning makes it difficult to reliably fit the model function to the data. This might result in erroneous values of the power ratio. Consequently, for the wavelength characterization presented in this paper, the power ratio is not a suitable measure. For the spot size calculation, however, the fitting procedure was used, but only to evaluate spots with high power ratios. The difference between the size values obtained using different fit functions (Airy disc and Gaussian function) is then also negligible in this wavelength range.

3. Results

3.1. Compensation of the SLM dispersion

The off-axis phase holograms displayed on the SLM consist of sums of blazed diffraction gratings. Therefore, they suffer from chromatic dispersion which causes a shift of the focused points corresponding to each individual grating in the Fourier plane of the SLM. Figure 2(a) shows the Fourier plane of the SLM for different wavelengths and the shift of the points caused by the dispersion and Fig. 2(b) shows the image of the Fourier plane at the fibre input facet. After the fibre is calibrated, when the wavelength is tuned, the whole pattern projected onto the input facet shifts and scales with wavelength, degrading the spot in the focal plane (Fig. 2(c)). Consequently, when such a system is used for imaging, the image contrast decreases as the wavelength is tuned.

Such dispersion of SLMs and DMDs in adaptive optics and beam scanning microscopy is a known problem, and more or less complicated solutions [20,23,24] have been suggested. Here, we additionally have the complication that we correct for many grating periods at the same time. We note that so far dispersion compensation has not been implemented for fibre imaging [15–17].

Two dispersion compensation techniques were tested in this paper. The first one uses a wedge prism placed at a plane conjugate with the SLM plane (here, just before the objective) to cancel the dispersion, and will be referred to as the *prism-based correction*. In our setup, the number of mirror reflections in the horizontal plane was even in one polarisation path and odd in the other. Therefore the dispersion in the second path was flipped and the dispersion occurred along the same axis for both polarisations (Fig. 2(b)). Thus, a single prism was sufficient to compensate for the dispersion in both polarisation paths. Although the prism compensates the dispersion for a range of wavelengths simultaneously, the compensation is only complete for a single wavelength (here chosen to be the calibration wavelength 780 nm). Hence, the method works only over a limited wavelength range, which, however, as we will show, gives a factor of 2 increase in the bandwidth compared to the uncompensated system. Moreover, for a given angle of incidence on the prism, the dispersion is correctly compensated only for a single SLM grating pitch. In the off-axis configuration, however, the pitch of all the gratings is similar. Therefore, this is not a severe limitation.

The second method is based on scaling the pitch of the individual gratings comprising the SLM pattern according to the grating equation and will be referred to as the *SLM-based correction*. This correction is more accurate than the prism-based correction, as it allows, in principle, correcting the hologram for an arbitrary wavelength over a broader wavelength range. However, since the scaling factor is wavelength dependent, the hologram must be corrected for every wavelength separately and therefore it is not suitable for use with a broadband source such as a femtosecond pulsed laser as it does not allow compensating for the dispersion across the whole bandwidth of the source. Moreover, in order to minimize the time to generate the holograms, the holograms are usually generated using a fast Fourier transform resulting in a discretised Fourier plane. Consequently, the dispersion can be corrected only at discrete wavelengths. In order to mitigate the impact of this discretisation on the measured data, the Fourier plane was significantly oversampled resulting in a near-continuous correction at the cost of reduced hologram generation speed.

Optics EXPRESS

The dispersion compensation techniques were compared using the tunable CW laser and a 50 mm long piece of high NA graded-index multimode fibre (Prysmian DrakaElite). First, the fibre was calibrated at a wavelength of 780 nm with a focal plane 50 µm in front of the fibre facet. Then, the laser wavelength was tuned and the intensity enhancement was measured in points forming a line across the fibre core. As shown in Figs. 2(c) and 2(d), both methods significantly broadened the usable wavelength tuning range. By disabling the gratings corresponding to one of the polarisations one at a time, it was verified that these results are independent on whether one or two input polarisations were used.

For the prism-based correction, the enhancement at the calibration wavelength is lower compared to that without any correction or with the SLM-based correction. This is a result of the high angle of incidence on the prism, which results in an elliptical beam (with a ratio of 1.5:1) in the back focal plane of the objective. This effect can, however, be mitigated by using a prism with a higher apex angle or made of a more dispersive material. Such a prism would allow a smaller angle of incidence resulting in a less elliptical beam.

Using the SLM-based correction allows us to measure the bandwidth of the fibre itself. To verify that we are indeed measuring the fibre bandwidth, we repeated the measurement for three fibres of different length — straight pieces that were 25 mm and 50 mm long and a 150 mm long fibre that had the shape of a loop. Because of the large radius of the loop, the bend of the fibre should not have an impact on its bandwidth [22,25]. Figures 3(a) and 3(b) show the intensity enhancement and the spot size at different wavelengths and spot positions for these three fibres. In these figures, an average value of the transverse and the longitudinal size is plotted for off-axis spots that are elliptical [26] and only the spot sizes smaller than 2.5 µm are plotted due to the limitation of the fitting procedure used for spot size calculation discussed above. The measured spot size at the calibration wavelength was 1.5 µm in the centre of the fibre, which is in reasonable agreement with the diffraction-limited spot size of 1.4 µm.

Figure 3(c) shows that the bandwidth (calculated as the FWHM of the enhancement measured as a function of the wavelength) of the fibre is inversely proportional to its length even for a 25 mm long fibre. That indicates that for fibres of this type that are longer than 25 mm, the bandwidth of the whole imaging system is limited by the fibre itself, not by the limits of the SLM-based correction method. In our setup, the bandwidth limit of the SLM-based correction method is above 44 THz.

As shown by the error bars in Fig. 3(c) that represent a standard deviation of the bandwidth values measured in a line across the whole fibre facet, the bandwidth does not depend on the position of the output point. Therefore, it is sufficient to compare the results only for an output point in the centre of the fibre facet. This result held also for the other fibres we tested.

The effect of dispersion correction is further demonstrated in Fig. 4. Here, a 1951 USAF resolution test chart was imaged in transmission. Without the dispersion correction, the contrast has dropped to half already at a wavelength 5 nm away from the calibration wavelength. This value, however, depends on the pitch of gratings used. For a fibre with a higher number of modes (i.e. for a fibre with a larger core diameter or higher numerical aperture), gratings with a smaller pitch would have to be used. This would result in a more rapid change of the pattern on the fibre with wavelength resulting in a smaller bandwidth. With the SLM-based dispersion correction, the image quality is the same at 5 nm and the contrast has dropped to half at 15 nm away from the calibration wavelength.

3.2. Bandwidth of different fibre types

To compare bandwidth between different types of fibre, four graded-index and one step-index fibre were tested using the technique described above, while the SLM-based correction was used. The results of the comparison are shown in Fig. 5 and summarized in Table 2. It should be noted that the specified bandwidth and the measured bandwidth in Table 2 are measured using different

Optics EXPRESS

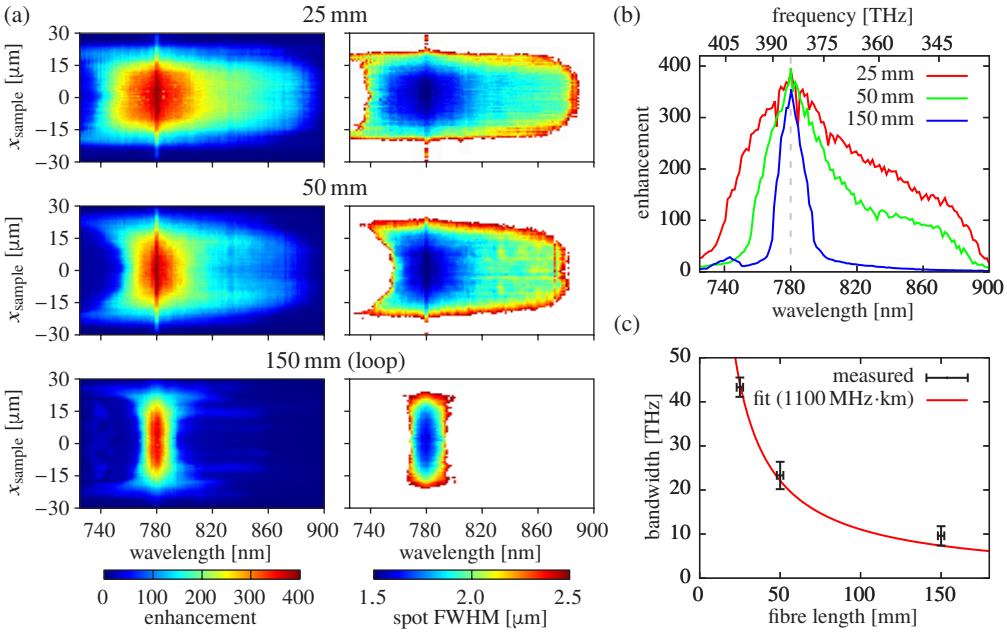

Fig. 3. Dependence of the bandwidth of a graded-index fibre (Prysmian DrakaElite) on its length. (a) Intensity enhancement and spot size (for spots ≤2.5 µm) as a function of the position of the output points (x_{sample}) and wavelength for three fibre lengths. (b) Comparison of the intensity enhancement for an output point in the centre of the facet. (c) Fibre bandwidth as a function of the fibre length. The vertical error bars show the standard deviation of the values measured in a line across the fibre facet and the horizontal error bars the uncertainty of the fibre length.

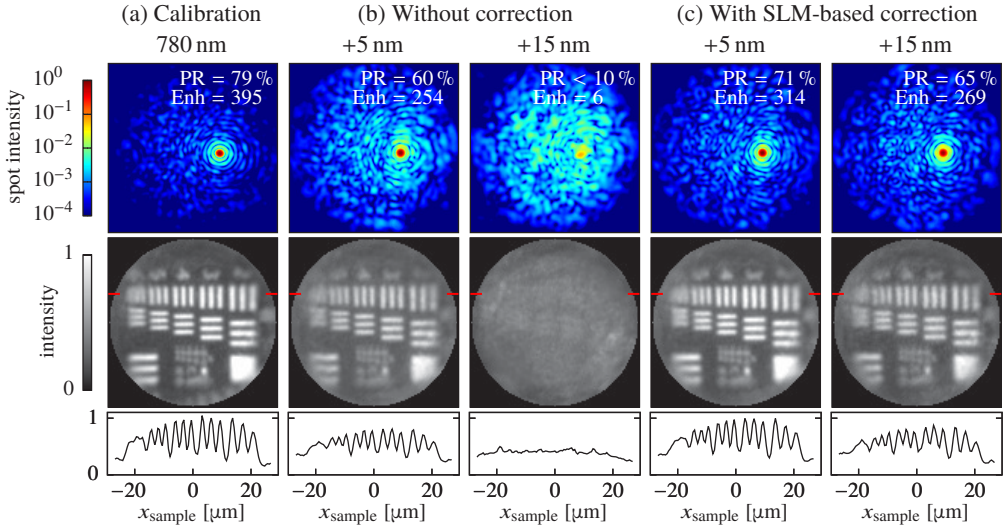

Fig. 4. Imaging with a graded-index fibre (Prysmian DrakaElite, 50 mm long) at different wavelengths with and without SLM-based dispersion correction. The top panels show a focused point at the imaging plane in a logarithmic scale (PR is the power ratio and Enh is the intensity enhancement). The middle panels show images of group 8 of a 1951 USAF resolution test chart, imaged in transmission. The bottom graphs are cross-sections of the images at the red mark.

Optics EXPRESS

techniques and for different wavelengths. In particular, the choice of wavelength can have a large effect on the bandwidth measurements [27], which further emphasizes the need for measuring the bandwidth for the imaging configuration used. As expected, the bandwidth of the step-index fibre is significantly lower than the bandwidth of any of the graded-index fibres. For most of the fibres tested the measured bandwidth at 780 nm is similar to the values specified at 850 nm. For the Prysmian DrakaElite fibre, however, the bandwidth is well above the specification, whereas for Thorlabs GIF50E fibre the measured bandwidth is significantly lower than specified. This is not due to a bandwidth limit of the optical setup itself, since, as discussed in the previous section and as shown in Fig. 3, the bandwidth of the setup it at least 44 THz, translating to at least 2200 MHz·km for a 50 mm long fibre.

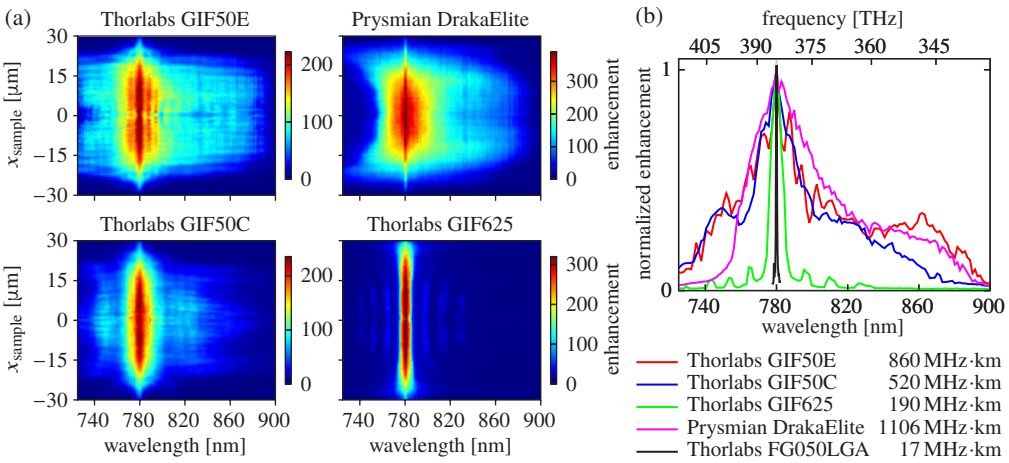

Fig. 5. Bandwidth for different fibre types. (a) Intensity enhancement for different output point positions (x_{sample}) after tuning from the calibration wavelength of 780 nm. All fibres were 50 mm long. (b) Comparison of different fibres for an output point at the centre of the facet. The values in the legend are the measured bandwidths.

Table 2. Specified and Measured Bandwidths of the Fibres Used in the Experiment. Parameters of the Fibres Are in Table 1.

Fibre	Type	Bandwidth	
		specified[a]	measured[b]
Thorlabs GIF50E	graded-index	3500 MHz·km	860 MHz·km
Thorlabs GIF50C	graded-index	700 MHz·km	520 MHz·km
Thorlabs GIF625	graded-index	≥ 200 MHz·km	190 MHz·km
Prysmian DrakaElite	graded-index	≥ 500 MHz·km	1106 MHz·km
Thorlabs FG050LGA	step-index	15 MHz·km	17 MHz·km

[a]Overfilled modal bandwidth at 850 nm (820 nm for the step-index fibre).
[b]For fibre imaging; measured using intensity enhancement at 780 nm.

The significant difference between the step-index and the graded-index fibres is further demonstrated in Fig. 6 which shows a focused point after wavelength tuning. For the step-index fibre, the axial position of the focused point changes significantly even for a small wavelength tuning, and for large wavelength changes, the point disappears completely. For all the graded-index fibres tested, the shift is insignificant and a much broader wavelength tuning range is usable without notable degradation of the focusing quality. The focusing quality in Fig. 5 is evaluated

Optics EXPRESS

in the same focal plane for all wavelengths. Any shift of the focused point along the fibre axis results in a decrease in the focusing quality. Consequently, step-index multimode fibres are not suitable for use as endoscopes for applications where broadband pulses have to be delivered into the sample or the laser wavelength needs to be tuned after the calibration. Complicated and lossy methods would be needed to deliver a short pulse to the focal plane [28], although specifically addressing the defocusing problem rather than a time-gated selection of modes as in [28] might be more efficient. The very narrow bandwidth of the SI fibre is also in line with the very narrow spectral widths measured in [29].

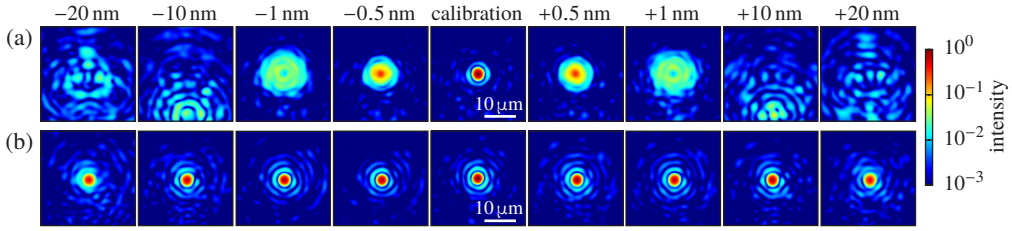

Fig. 6. A focused point plotted in a logarithmic scale at the focal plane after wavelength tuning from the calibration wavelength for (a) the step-index fibre (Thorlabs FG050LGA) and (b) a graded-index fibre (Thorlabs GIF50E). SLM-based dispersion correction was used.

The technique for measuring the fibre bandwidth described above is capable of determining all the imaging properties of the fibre (including the achievable spot size), however, it requires calibrating the fibre imaging system and compensating for the chromatic dispersion of the hologram. Consequently, another method based on speckle pattern decorrelation [30] was investigated. In this method, a single focused point was created on the input fibre facet and speckle patterns created at the focal plane in front of the output fibre facet were recorded while the laser was tuned and compared (using an intensity correlation coefficient) with a speckle pattern captured at the calibration wavelength. The focused input point was in our case created by the SLM and thus its dispersion had to be compensated. It is, however, sufficient to create it with lenses only. Figure 7 shows a comparison of both methods for two different fibres. The correlation coefficient was normalised so that value 1 corresponds to a correlation of two identical speckle patterns and value 0 corresponds to a correlation between speckle patterns at two distinctly different wavelengths separated by significantly more than the fibre bandwidth. Both techniques show comparable results in terms of bandwidth measurement. The latter one, however, cannot evaluate all the properties of the focused point, thus it cannot describe the imaging performance of the endoscope accurately.

The speckle correlation is, however, useful for comparing the measurements with modelling. We compared the experimental results with simulations of idealized optical fibres. For each wavelength in the study, we found the exact fibre modes by numerically solving the eigenproblem for the transverse wave equation for the magnetic field with an appropriate, circularly symmetric, index profile. The model fibre was illuminated with a Gaussian spot (waist radius 1 µm, centre at $x = 15$ µm), whose modal expansion coefficients were found by projection onto the calculated fibre modes. The spot was propagated through the fibre according to the modal propagation constants from the eigenproblem. The Pearson correlation coefficient between the speckle at 780 nm and at neighbouring wavelengths was evaluated. Figure 7 shows the comparison between theory and experiment. Model results reproduce the prominent features of the experiment i.e. when estimated in this way, the bandwidths for graded-index fibres are much wider than they are for step-index fibres. Since the calculations are exact, for ideal fibres, differences between theory and experiment can be attributed to imperfections in the experimental fibres. Finally, we note the need for exact calculations of the fibre modes. Performing similar calculations

Optics EXPRESS

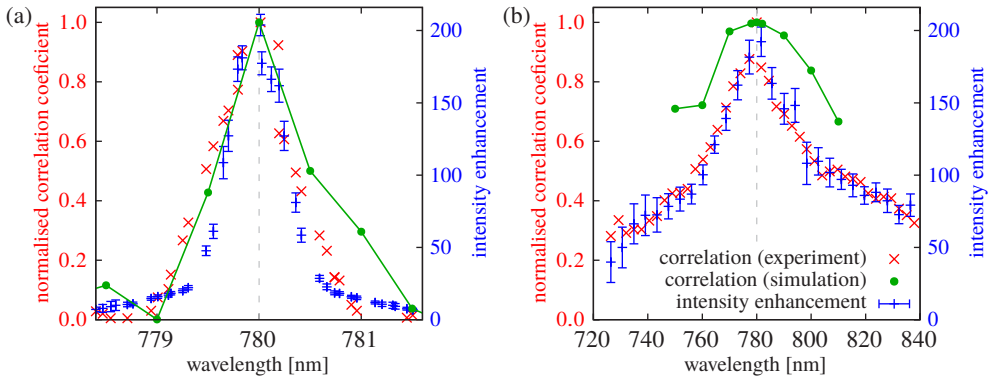

Fig. 7. Comparison of two techniques for fibre bandwidth measurement (intensity enhancement measurement in the focused output point and speckle decorrelation measurement) for (a) the step-index fibre (Thorlabs FG050LGA) and (b) a graded-index fibre (Thorlabs GIF50E). The error bars for the enhancement show a standard deviation across a 30 µm long line centred at the fibre axis. The lines in the simulation results are a guide to the eye.

under the scalar approximation, for example, does not compare well with the experiments for graded-index fibres. Under this approximation, the initial spot is repeatedly refocused owing to a particular relationship between the approximate propagation constants and propagation through the fibre does not generate speckle. A similar effect is observed for the exact treatment, but the fidelity of the focus deteriorates with propagation distance and speckle patterns emerge after several centimetres. It is these deviations from the scalar approximation that, at least partially, account for the bandwidth of real graded-index fibres. In the experiments, we do not observe the self-imaging effect. This likely points to that the light propagation through the graded-index fibres are more influenced by imperfections and scatterers that can be reproduced in the model. This is in contrast to the step-index fibres, where the model produces results that are more similar to the experiments.

3.3. *Femtosecond pulse focusing*

To illustrate the effect of the fibre bandwidth on focusing a broadband pulse through a multimode fibre, the calibration procedure was performed using the femtosecond laser for three different 50 mm long fibres with different bandwidths. The SLM dispersion was not compensated during the experiment since for the chosen range of gratings, the bandwidth of the system was higher than the laser spectral width. For a more broadband source, however, it would be necessary to use the prism-based correction method.

Figure 8(a) shows examples of the focused output points obtained for the three fibre types. For the Prysmian DrakaElite fibre, the bandwidth of the imaging system was limited by the SLM dispersion. Despite that, it was higher than the spectral width of the laser (Fig. 8(b)) and the spot had a very little speckle background. For the Thorlabs GIF625 fibre, the bandwidth was limited by the fibre itself and was smaller than the laser spectral width. The speckle background around the spot started to be visible and the power ratio dropped to 45 %. Since the bandwidth of the fibre is inversely proportional to its length (as shown in Fig. 3), for a longer fibre, the bandwidth of the Thorlabs GIF625 fibre would not be sufficient and the speckle background would increase. To illustrate the effect this would have, we focused the pulse through the step-index fibre, which has a significantly lower bandwidth than the spectral width of the laser. Clearly, the focus is very poor. This illustrates that it is critical to choose a fibre with sufficient bandwidth.

Optics EXPRESS

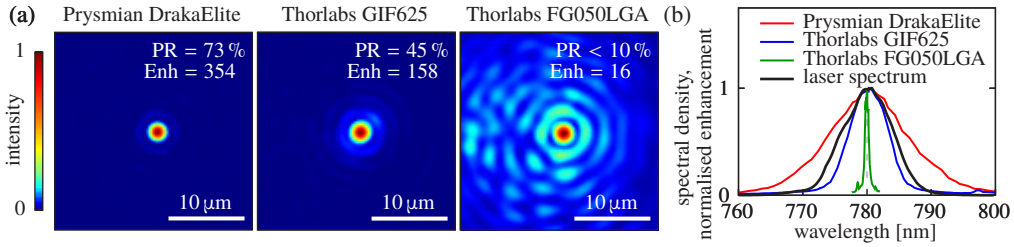

Fig. 8. Focusing the femtosecond laser through a multimode fibre. (a) Focused output points created with three different fibres — with higher, similar and lower bandwidth compared to the laser spectral width. PR is the power ratio and Enh is the intensity enhancement. (b) Comparison of the laser spectrum and the bandwidth of the entire system. No SLM dispersion compensation was used.

3.4. Spectral phase

When focusing a broadband pulse through a multimode fibre endoscope, the pulse broadens due to material dispersion and residual modal dispersion. For non-linear imaging that requires high peak powers, it is, therefore, necessary to compensate for the dispersion in order to obtain transform-limited pulses in the sample plane. To study how the multimode fibre affects the dispersion of the imaging system, the spectral phase of the output points was measured.

We note that other methods are available for completely characterizing the pulse from a multimode fibre [31], without creating a focus first, although these might be harder to implement for fibres with a large number of modes. In addition, for the graded-index fibres, as we will show, this is a sufficient method.

After the calibration procedure, focused output points were created in the focal plane located 50 µm in front of the fibre output facet or 50 µm in front of the first objective focal plane in case of measuring the dispersion without the fibre. Then, the image of the output point on the camera was overlapped with a plane reference wave. Using phase-shifting interferometry, both the spectral phase (relative to the reference wave) and amplitude were measured for all points in the whole focal plane simultaneously. This method would, therefore, allow investigations of spatiotemporal couplings in the focused spot. Here, the spectral phase of the output point was determined as a phase in the pixel with maximal amplitude. The measurement was then repeated for different wavelengths and the output point positions using the same calibration and the prism-based dispersion correction method. The measured phase values were unwrapped and the constant and linear terms (corresponding to an optical path difference between the two optical paths) were subtracted (Fig. 9(a)). The experiment was repeated for two different fibre lengths.

To calculate the dispersion of the fibre, the experiment was performed with no fibre in the setup. The calibration procedure normally associated with the multimode fibres was then used to compensate for the aberrations in the setup (mainly an astigmatism caused by the wedge prism). By subtracting the phase measured with and without the fibre, the dispersion of the fibre itself was obtained. As shown in Fig. 9(b), the dispersion caused by the fibre is purely second-order in the wavelength range used and it scales linearly with the fibre length. The group velocity dispersion of the fibre calculated from the fit is 50 $fs^2 \cdot mm^{-1}$ at 780 nm and does not depend on the output point position or the fibre length. This clearly shows that it would be sufficient to correct for the dispersion of the fibre once for a specific fibre length and that there is no need to correct for the dispersion in between different sample positions in an imaging experiment. The measured group velocity dispersion of the fibre is higher than the value for fused silica (38 $fs^2 \cdot mm^{-1}$), which is caused by the doping of the fibre core.

Optics EXPRESS

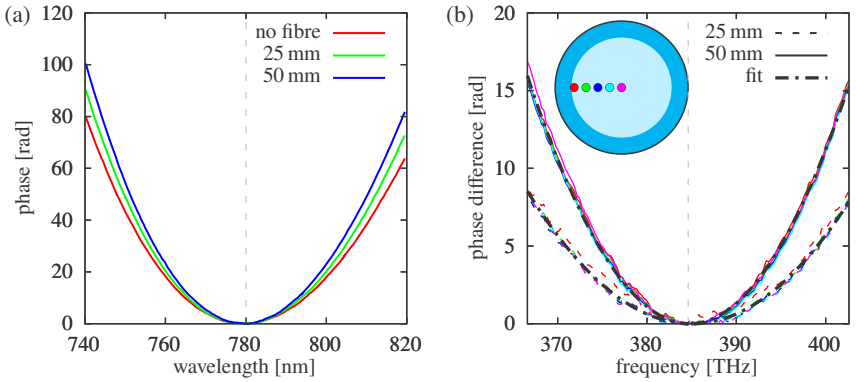

Fig. 9. Spectral phase measurement results for Prysmian DrakaElite fibre. (a) Spectral phase of a focused output point in the focal plane measured without the fibre and with two different fibre lengths. (b) Phase after subtracting values without the fibre for different spot positions. The fit is a quadratic function (corresponding to a second-order dispersion).

4. Summary

In this paper, the bandwidth of a multimode fibre imaging system and its impact on focusing both CW and femtosecond laser beams was investigated.

In general, there are two bandwidth limiting factors in multimode fibre imaging systems. The first arises from the fact that the off-axis phase holograms displayed on the SLM have the form of sums of diffraction gratings and therefore suffer from chromatic dispersion. The dispersion then causes a change of the pattern projected onto the fibre facet resulting in a decrease of the quality of the focus. The dispersion of the hologram can, however, be corrected. Consequently, two dispersion compensation methods were tested. One method is purely optical and is based on compensating the grating dispersion using a prism. This technique compensates the dispersion simultaneously for a range of wavelengths and is therefore suitable for use with femtosecond pulses. For the CW laser, it allows a wavelength tuning range (bandwidth, calculated as the FWHM of the intensity enhancement measured as a function of the wavelength) of 34 nm (17 THz) around the calibration wavelength of 780 nm using a 50 mm long Prysmian DrakaElite fibre. The other method is based on correcting the phase holograms on the SLM according to the grating equation. Since the hologram has to be generated separately for each wavelength, it is not suitable for use with broadband sources. Using this method and the CW laser, the bandwidth of the imaging system was >47 nm (23 THz). Without any correction, the bandwidth was only 14 nm (7 THz). This value, however, depends on the pitch of the gratings used and would be lower if a fibre with more modes (i.e. with a larger core diameter or higher NA) is used. As we demonstrated, the uncompensated system allows focusing of a 100 fs pulse making it suitable for e.g. two-photon imaging at a single wavelength with a laser typically used for bio-imaging. The extended wavelength range would be useful, for instance, for imaging multiple dyes at different excitation wavelengths or for CARS (Coherent anti-Stokes Raman Scattering) imaging, where images at multiple Raman shifts could be acquired using the same calibration. For CARS used for bio-imaging, a typical tuning range would be 250 cm^{-1}, i.e., ≈15 nm. If a femtosecond laser is used for CARS, additional bandwidth is required in order to accommodate the laser spectral width.

The other bandwidth-limiting component in the system is the multimode fibre. While the dispersion of the hologram can be corrected for, the limited bandwidth of the fibre cannot be easily overcome. Therefore, the choice of the fibre is crucial, because it limits not only the ability to tune the wavelength after the calibration procedure without degrading the imaging

Optics EXPRESS

properties but, more importantly, the ability to focus light from a broadband source such as a femtosecond laser. In general, graded-index fibres have higher bandwidth than step-index fibres. The exact bandwidth values, however, depend on the wavelength, fibre type and also on its length. We found that at 780 nm, the fibres suitable for broadband pulse focusing were the Prysmian DrakaElite, Thorlabs GIF50C and GIF50E. All of these fibres have sufficient bandwidth to focus a transform-limited 100 fs pulse for a fibre length of 50 mm. We also demonstrated that using a fibre with a bandwidth only slightly lower than the bandwidth of the laser substantially reduces the power ratio.

In addition, the spectral phase of the output points was measured. The GVD of the Prysmian DrakaElite fibre was measured to be 50 $fs^2 \cdot mm^{-1}$ at 780 nm. This value did not depend on the position of the output point. This implies that a standard method for dispersion compensation, such as a prism compressor, is sufficient for multi-photon imaging with a fibre endoscope.

Funding

European Regional Development Fund (CZ.02.1.01/0.0/0.0/15_003/0000476); Ministerstvo Školství, Mládeže a Tělovýchovy (LO1212); European Commission (CZ.1.05/2.1.00/01.0017); Akademie Věd České Republiky (RVO:68081731).

Acknowledgment

Prysmian Group is gratefully acknowledged for the high NA graded-index fibre sample. Petr Jákl is acknowledged for the development of the camera toolbox.

References

1. L. V. Amitonova, A. Descloux, J. Petschulat, M. H. Frosz, G. Ahmed, F. Babic, X. Jiang, A. P. Mosk, P. S. Russell, and P. W. H. Pinkse, "High-resolution wavefront shaping with a photonic crystal fiber for multimode fiber imaging," Opt. Lett. **41**(3), 497–500 (2016).
2. I. T. Leite, S. Turtaev, X. Jiang, M. Šiler, A. Cuschieri, P. S. J. Russell, and T. Čižmár, "Three-dimensional holographic optical manipulation through a high-numerical-aperture soft-glass multimode fibre," Nat. Photonics **12**(1), 33–39 (2018).
3. S. A. Vasquez-Lopez, R. Turcotte, V. Koren, M. Plöschner, Z. Padamsey, M. J. Booth, T. Čižmár, and N. J. Emptage, "Subcellular spatial resolution achieved for deep-brain imaging in vivo using a minimally invasive multimode fiber," Light: Sci. Appl. **7**(1), 110 (2018).
4. S. Ohayon, A. Caravaca-Aguirre, R. Piestun, and J. J. DiCarlo, "Minimally invasive multimode optical fiber microendoscope for deep brain fluorescence imaging," Biomed. Opt. Express **9**(4), 1492–1509 (2018).
5. S. Turtaev, I. T. Leite, T. Altwegg-Boussac, J. M. P. Pakan, N. L. Rochefort, and T. Čižmár, "High-fidelity multimode fibre-based endoscopy for deep brain in vivo imaging," Light: Sci. Appl. **7**(1), 92 (2018).
6. I. M. Vellekoop and A. P. Mosk, "Focusing coherent light through opaque strongly scattering media," Opt. Lett. **32**(16), 2309–2311 (2007).
7. S. Rotter and S. Gigan, "Light fields in complex media: Mesoscopic scattering meets wave control," Rev. Mod. Phys. **89**(1), 015005 (2017).
8. T. Čižmár and K. Dholakia, "Shaping the light transmission through a multimode optical fibre: Complex transformation analysis and applications in biophotonics," Opt. Express **19**(20), 18871–18884 (2011).
9. T. Čižmár and K. Dholakia, "Exploiting multimode waveguides for pure fibre-based imaging," Nat. Commun. **3**(1), 1027 (2012).
10. I. N. Papadopoulos, S. Farahi, C. Moser, and D. Psaltis, "High-resolution, lensless endoscope based on digital scanning through a multimode optical fiber," Biomed. Opt. Express **4**(2), 260–270 (2013).
11. M. Plöschner, V. Kollárová, Z. Dostál, J. Nylk, T. Barton-Owen, D. E. K. Ferrier, R. Chmelík, K. Dholakia, and T. Čižmár, "Multimode fibre: Light-sheet microscopy at the tip of a needle," Sci. Rep. **5**(1), 18050 (2015).
12. Y. Choi, C. Yoon, M. Kim, T. D. Yang, C. Fang-Yen, R. R. Dasari, K. J. Lee, and W. Choi, "Scanner-Free and Wide-Field Endoscopic Imaging by Using a Single Multimode Optical Fiber," Phys. Rev. Lett. **109**(20), 203901 (2012).
13. S. Deng, D. Loterie, G. Konstantinou, D. Psaltis, and C. Moser, "Raman imaging through multimode sapphire fiber," Opt. Express **27**(2), 1090–1098 (2019).
14. I. Gusachenko, M. Chen, and K. Dholakia, "Raman imaging through a single multimode fibre," Opt. Express **25**(12), 13782–13798 (2017).
15. E. E. Morales-Delgado, D. Psaltis, and C. Moser, "Two-photon imaging through a multimode fiber," Opt. Express **23**(25), 32158–32170 (2015).

Optics EXPRESS

16. S. Sivankutty, E. R. Andresen, R. Cossart, G. Bouwmans, S. Monneret, and H. Rigneault, "Ultra-thin rigid endoscope: Two-photon imaging through a graded-index multi-mode fiber," Opt. Express **24**(2), 825–841 (2016).
17. E. Kakkava, M. Romito, D. B. Conkey, D. Loterie, K. M. Stankovic, C. Moser, and D. Psaltis, "Selective femtosecond laser ablation via two-photon fluorescence imaging through a multimode fiber," Biomed. Opt. Express **10**(2), 423–433 (2019).
18. T. Meyer, M. Chemnitz, M. Baumgartl, T. Gottschall, T. Pascher, C. Matthäus, B. F. M. Romeike, B. R. Brehm, J. Limpert, A. Tünnermann, M. Schmitt, B. Dietzek, and J. Popp, "Expanding Multimodal Microscopy by High Spectral Resolution Coherent Anti-Stokes Raman Scattering Imaging for Clinical Disease Diagnostics," Anal. Chem. **85**(14), 6703–6715 (2013).
19. M. Plöschner, T. Tyc, and T. Čižmár, "Seeing through chaos in multimode fibres," Nat. Photonics **9**(8), 529–535 (2015).
20. J. Leach, G. M. Gibson, M. J. Padgett, E. Esposito, G. McConnell, A. J. Wright, and J. M. Girkin, "Generation of achromatic Bessel beams using a compensated spatial light modulator," Opt. Express **14**(12), 5581–5587 (2006).
21. Z. Wu, J. Luo, Y. Feng, X. Guo, Y. Shen, and Z. Li, "Controlling 1550-nm light through a multimode fiber using a Hadamard encoding algorithm," Opt. Express **27**(4), 5570–5580 (2019).
22. S. Farahi, D. Ziegler, I. N. Papadopoulos, D. Psaltis, and C. Moser, "Dynamic bending compensation while focusing through a multimode fiber," Opt. Express **21**(19), 22504–22514 (2013).
23. M. Hoffmann, I. N. Papadopoulos, and B. Judkewitz, "Kilohertz binary phase modulator for pulsed laser sources using a digital micromirror device," Opt. Lett. **43**(1), 22–25 (2018).
24. Q. Geng, C. Gu, J. Cheng, and S.-C. Chen, "Digital micromirror device-based two-photon microscopy for three-dimensional and random-access imaging," Optica **4**(6), 674–677 (2017).
25. D. E. Boonzajer Flaes, J. Stopka, S. Turtaev, J. F. de Boer, T. Tyc, and T. Čižmár, "Robustness of Light-Transport Processes to Bending Deformations in Graded-Index Multimode Waveguides," Phys. Rev. Lett. **120**(23), 233901 (2018).
26. R. N. Mahalati, R. Y. Gu, and J. M. Kahn, "Resolution limits for imaging through multi-mode fiber," Opt. Express **21**(2), 1656–1668 (2013).
27. E. R. Parsons, R. Patterson, J. Young, and P. F. Kolesar, "The Impact of Effective Modal Bandwidth on 100G SWDM Transmission Over 250 m OM5 and Left-Tilt OM4 Multimode Fibers," J. Lightwave Technol. **36**(24), 5841–5848 (2018).
28. E. E. Morales-Delgado, S. Farahi, I. N. Papadopoulos, D. Psaltis, and C. Moser, "Delivery of focused short pulses through a multimode fiber," Opt. Express **23**(7), 9109–9120 (2015).
29. B. Redding, S. M. Popoff, and H. Cao, "All-fiber spectrometer based on speckle pattern reconstruction," Opt. Express **21**(5), 6584–6600 (2013).
30. B. Moslehi, J. W. Goodman, and E. G. Rawson, "Bandwidth estimation for multimode optical fibers using the frequency correlation function of speckle patterns," Appl. Opt. **22**(7), 995–999 (1983).
31. P. Zhu, R. Jafari, T. Jones, and R. Trebino, "Complete measurement of spatiotemporally complex multi-spatial-mode ultrashort pulses from multimode optical fibers using delay-scanned wavelength-multiplexed holography," Opt. Express **25**(20), 24015–24023 (2017).